

Modeling non-Darcy flows in realistic pore-scale proppant geometries

Anna Trykozko¹, Malgorzata Peszynska², and Marek Dohnalik³

¹Interdisciplinary Centre for Mathematical and Computational Modelling,
University of Warsaw, Pawinskiego 5a, 02-106 Warsaw, Poland
(A.Trykozko@icm.edu.pl)

²Department of Mathematics, Oregon State University, Corvallis, OR 97330,
USA (mpesz@math.oregonstate.edu)

³Institute of Oil and Gas, ul. Bagrowa 1, 30-733 Kraków, Poland
(dohnalik@inig.pl)

Abstract. The ability to evaluate the effective permeability of proppant packs is useful in predicting the efficiency of hydraulic fracture installations. In this paper we propose a computational approach combining microimaging data from X-ray computed microtomography, the simulations of flow at pore-scale, and an upscaling process which identifies the effective model parameters at the core-scale. With this computational approach applied to proppant pack we confirm the reduction in the fracture conductivity and subsequent reduction in the productivity of a hydraulically fractured reservoir due to the high flow rates and to the migration of fine particles resulting in pore throat bridging.

Keywords: pore-scale simulations, non-Darcy flows, conductivity

1 Introduction

Computational modeling of flow at pore-scale is a powerful tool providing insight into the character of flow in complex pore-scale geometries composed of grains and voids. When combined with upscaling, the pore-scale simulations can provide effective parameters characterizing the flow at core-scale, which can be subsequently used in reservoir scale models. Pore-scale computations are especially meaningful in realistic 3D geometries such as those obtained by X-ray computed microtomography and other microimaging techniques [1, 2, 3], but they remain a challenging computational task. Direct Numerical Simulations (DNS), i.e., direct numerical discretization of partial differential equations describing the flows at pore-scale are increasingly popular [4, 1, 5, 6, 7, 8, 9] since they can be easily coupled to simulate processes other than just the flow.

In this work we apply DNS at pore-scale and our method of upscaling developed and refined in [10, 11, 12, 7, 13] to study the flow through a proppant pack. We describe the methodology

Published in: *Computers and Geotechnics*, Vol. 71, (2016), 352-360, doi: 10.1016/j.compgeo.2015.08.011.

©2015 This manuscript version is made available under the CC-BY-NC-ND 4.0 license <http://creativecommons.org/licenses/by-nc-nd/4.0/>.

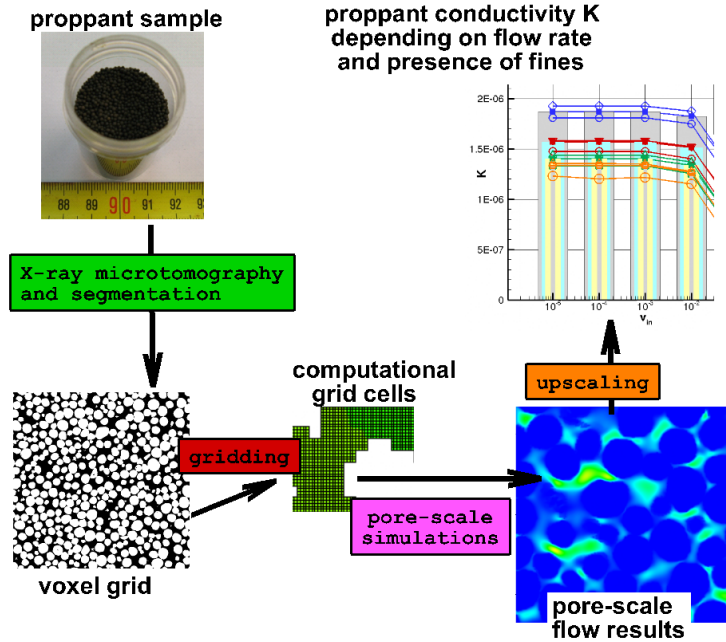


Figure 1: The schematic workflow in our “virtual lab”. The arrows indicate different steps described in this paper.

which starts with a realistic geometry obtained by microimaging and which helps to assess the critical factors determining the efficiency of hydraulic fracturing such as the fracture and proppant conductivities. The process is shown schematically in Figure 1.

Hydraulic fracturing of oil and gas wells creates highly conductive fractures that connect the reservoir to a well and enables sustained production. This complex process [14, 15, 16]. starts by injecting fluid into a formation under high pressure which induces fracturing. In order to keep the walls of fractures open after injection stops, small solid particles called proppant are added to the injected fluid. An optimal fluid system must be able not only to extend the fracture length, but also to transport the proppant.

There is a big variety of materials used to prop the fractures open. These may be natural (sand), or manufactured particles (ceramics, resin-coated silica, bauxite). The proppant material is selected depending on several criteria, mostly related to the reservoir lithology. Critical factors are closure stresses and fracture conductivity requirements.

Factors that negatively impact the fracture conductivity also negatively impact the well productivity. The fracture conductivity depends on fracture width and on the conductivity of the embedded proppant filled domain, which affects the overall fracture conductivity significantly at a smaller scale. It is difficult to measure fracture conductivities in a lab due to the scales involved as well as due to the difficulties in mimicking the realistic process conditions such as high temperature and pressure and large flow rates. Frequently the values measured overpredict the realistic conductivities by an order of magnitude [16].

In this paper we use pore-scale simulations to study various factors affecting proppant conductivity and its reduction. In particular we are interested in conductivity reduction due to non-Darcy effects at high flow rates. The influence of high flow rates on productivity of wells



Figure 2: Ceramic proppant used in this paper. Grain size is within the range $600\ \mu\text{m}$ – $1180\ \mu\text{m}$ (mesh 16/30).

has been studied for a long time [17]; see also theoretical and computational models in [18, 19] and references therein. We study this aspect of proppant conductivity following our prior work on glass beads, sandstone, and synthetic geometries in [11, 7, 13, 12].

We also consider another factor causing a reduction in fracture conductivities due to the migration of fine particles (fines). The propping fluid, if not cleaned up, causes cyclic stress resulting in crushing, fines migration and intrusion as well as proppant scaling. Subsequently the geometry of voids and grains in the proppant may be altered by several overlapping mechanisms of particle deposition such as surface deposition, pore-throat bridging, internal cake formation, or particle accumulation in low flow regions [14]. Here we consider a model of bridging throats in the proppant and describe the associated reduction of conductivity.

The paper is organized as follows. Section 2 describes the microimaging data obtained for a proppant sample. In Section 3 we describe the computational pore-scale and upscaling approaches. In Section 4 we present the results of computational experiments. We demonstrate the conductivity reduction due to (i) high flow rates, and to (ii) the bridging of throats simulated with a stochastic model.

2 Microimaging and proppant pore-scale geometry

X-ray computed tomography is a non-destructive technique enabling 3D reconstructions of the internal structure of various objects, and this technique has been used very successfully to obtain images of pore-scale geometries [1, 2]. In this paper we are concerned with the simulations of flow in a proppant pack sample obtained from X-ray computed microtomography.

A sample of ceramic proppant with the grains of diameters varying from $600\ \mu\text{m}$ to $1180\ \mu\text{m}$ (mesh 16/30), Fig. 2 was imaged with the Benchtop CT-160X X-ray microtomograph [20, 21]. The measurements were performed under 130 kV energy of the X-ray source and the current

Table 1: Classification of voids

Volume Class	Class Volume [voxel]	Volume [μm^3]	Isolated Objects Counts	Class Volume [voxel]
I	1–9	5929 - 53367	0	0
II	10–99	$5929 \times 10^1 - 5929 \times 10^2$	1556	37249
III	100–999	$5929 \times 10^2 - 5929 \times 10^3$	48	9044
IV	1000–9999	$5929 \times 10^3 - 5929 \times 10^4$	1	1114
V	10000–99999	$5929 \times 10^4 - 5929 \times 10^5$	0	0
VI	100000–999999	$5929 \times 10^5 - 5929 \times 10^6$	0	0
VII	>1000000	$> 5929 \times 10^6$	1	232458000

70 μA conditions. In order to perform a full scan the sample was rotated by 360° and 2203 projections were registered. The final projection was averaged from two frames, and for each frame the 708 ms exposure time was applied. To avoid beam hardening artefact, a 0.4 mm copper filter was used. The collected projections were reconstructed with the CT Pro software [22]. During this step the sequence of projections was transformed into a 3D description, consisting of a set of two-dimensional grey-scale images, representing parallel equidistant cross sections along the sample. Data was then segmented with AVIZO software [23] to lead finally to a binary representation of a medium made of the voids and the solids.

As a result of the microimaging procedure a set of 600 cross sections was obtained, each consisting of 1000×1000 voxels with the unit voxel resolution $h = 18.1 \times 10^{-6}\text{m}$. In this way the geometry of a porous sample is described by a matrix of voxels:

$$n_{ijk} = \begin{cases} 0 & \text{cell is available to fluid,} \\ 1 & \text{cell is occupied by rock.} \end{cases} \quad (1)$$

Geometric properties of the pore structure image were further analysed with the use of MAVI software [24]. The analysis confirmed the connectivity of voids in x , y , and z directions. The classification of voids showed that the structure consists of one large connected system constituting almost 100% of the volume of voids. In addition, 1605 small isolated groups of voids were detected. In Table 1 we provide detailed geometrical information about the sample; this information is later complemented by the insight from the computational approaches described below.

3 Computational modeling of flows at pore-scale and up-scaling to core-scale

In this section we overview the simulations at pore-scale as well as our upscaling methodology which are central to the workflow shown in Figure 1. We consider a core sample $\Omega \subset \mathbf{R}^3$ of porous medium, in which we recognize two subregions, the flow domain Ω_F made of pores (also referred to as voids), and the solid domain Ω_S made of (proppant) grains. We have $\Omega = \Omega_F \cup \Omega_S \cup \Gamma$, where $\Gamma = \partial\Omega_F \cap \partial\Omega_S$ is the solid-fluid interface. See Figure 3 for illustration.

The pore-scale flow occurs in Ω_F only and we assume it is governed by the steady-state incompressible Navier–Stokes equations

$$\rho \mathbf{v} \cdot \nabla \mathbf{v} - \mu \nabla^2 \mathbf{v} = -\nabla p, \quad x \in \Omega_F, \quad (2)$$

$$\nabla \cdot \mathbf{v} = 0, \quad x \in \Omega_F, \quad (3)$$

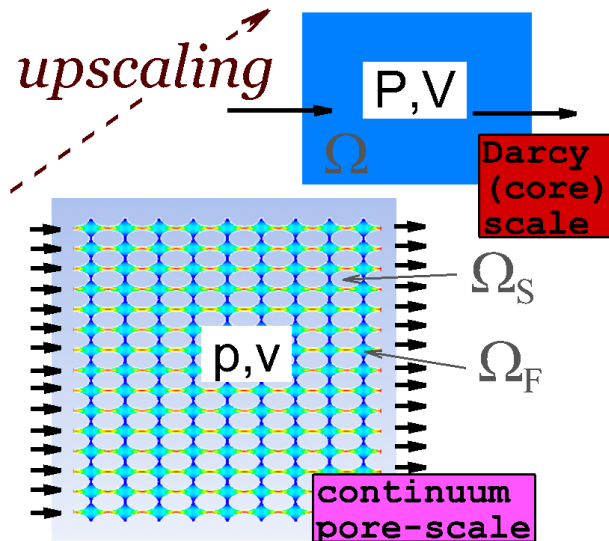


Figure 3: Illustration of pore-scale and core-scale geometries.

in which the pressures p [Pa] and the velocity \mathbf{v} [m/s] are the unknowns. Here ρ [kg/m³] denotes fluid density, and μ [kg/m · s] is kinematic viscosity of the fluid.

In complex geometries such as Ω_F solving Navier–Stokes equations (2)-(3) is very challenging but possible. Direct Numerical Simulations (DNS) of (2)-(3) on realistic pore-scale geometries were reported in the last decade [25, 4, 5, 26, 27, 8, 7, 9, 6] and they seem to gain popularity over the alternatives such as Pore-network method [28, 29]. The latter uses a reduced representation of Ω_F and thus can be inaccurate, especially when the pore and the grain sizes are similar.

In our approach [10, 11, 12, 7, 13] we use DNS followed by upscaling to determine the core-scale parameters, and the main ingredients of our virtual laboratory are as follows. First (i) we obtain a computational mesh over Ω_F from the voxel-based pore-scale geometry (1), typically given by X-ray computed microtomography. Second, (ii) we use fluid dynamics software; in this paper we use the Finite Volume based ANSYS/Fluent model [30]. Third, we follow with (iii) upscaling and identification of the core-scale model parameters. Details are provided below.

Computational meshes In general, dealing with realistic 3D geometries at pore-scale requires a compromise between a resolution at which the medium is represented and the size of a computational discretized problem.

Realistic 3D geometries of pore-scale flow domain Ω_F require a complex computational mesh with many grid cells. For voxel geometries the most natural grid type is an unstructured collection of regular hexahedral cells; see [4, 5, 26, 27, 8]. Another option of a body-fitted mesh as in [6] is possible but does not significantly affect the solutions as shown in [7, 9].

For large samples Ω the number of void voxels n_{ijk} can be easily of the order of more than $O(10^8)$, which makes solving (2)-(3) very difficult. Two approaches help to reduce the size of the computational problem. The first approach is the reduction or coarsening which consists of replacing a set of adjacent $2 \times 2 \times 2 = 8$ voxels forming a box with one (larger) voxel defined as a solid if the majority of the original voxels are of solid type, and as void otherwise. Such coarsening or averaging can be performed several times, reducing the size of data but also the

resolution by about an order of magnitude. The second way to reduce the computational problem to a manageable size is to consider only a subdomain of the original image data Ω_F . This approach gives satisfactory results provided the sample is representative, in agreement with the *Representative Elementary Volume* (REV) concepts [31, 5]. The two approaches of data reduction can be applied simultaneously to yield a reduced Ω_F .

The actual computational mesh over Ω_F requires one more step to avoid having only one mesh cell in some narrow pore throats. For this, we require at least one level of grid refinement.

Setting up flow simulations The Navier-Stokes model (2)-(3) must be complemented with boundary conditions. In our computational experiments we prescribe (a) the Dirichlet value v_{in} of velocity on the boundary $\partial\Omega_F$ of Ω_F with one external side of the region Ω chosen as the inflow side. Next we identify the opposite side of Ω as the outflow side, and there we impose (b) the pressure outflow condition. We also impose (c) the no-slip boundary condition (wall boundary condition) on all remaining external sides of the sample and on all fluid-solid interfaces Γ within the sample.

Upscaling to core-scale The simulations at pore-scale provide detailed information about the pointwise values of pressures $p(x)$ and velocities $\mathbf{v}(x)$ for every point x in the flow domain Ω_F . However, our main interest is to obtain core-scale parameters. The core-scale parameters we obtain computationally can be used in the reservoir models instead of experimental values, and recently we showed in [32] that there is a good agreement between the computations and experiment.

At the macro-scale the variables describing the flow are the macroscopic pressure P and velocity \mathbf{V} defined on Ω , in contrast to the pore-scale variables p and \mathbf{v} which are defined in Ω_F . The variables P and \mathbf{V} are commonly defined as local averages of p and \mathbf{v} [31].

The mass conservation at macroscale is similar to (3),

$$\nabla \cdot \mathbf{V} = 0, \quad x \in \Omega. \quad (4)$$

The momentum conservation relates P and \mathbf{V} for slow flow rates via well-known Darcy's law

$$\mathbf{V} = -\mathbf{K}\nabla P = -\frac{\mathbf{k}}{\mu}\nabla P, \quad x \in \Omega, \quad (5)$$

where $\mathbf{K} = \frac{\mathbf{k}}{\mu}$ [$\text{m}^2/\text{Pa} \cdot \text{s}$] is the Darcy conductivity, and \mathbf{k} [m^2] the absolute (intrinsic) permeability. \mathbf{K} and \mathbf{k} are symmetric positive definite tensors.

The fine scale information about the geometry of Ω_F is not lost in (5) because it is “encoded” in the values of the conductivity \mathbf{K} . The aim of upscaling is to provide the connection between Ω_F and \mathbf{K} ; see the theoretical derivations in [31, 33] and more recent work in [34, 35]. We realize this process computationally following the ideas of [36] which we refined for the needs of pore-to-core upscaling in [10, 11, 7, 13] as explained below.

After Equations (2)-(3) are solved computationally for the pore-scale pressure p and velocity \mathbf{v} , they are averaged over particularly chosen subregions of Ω ; this step gives the core-scale counterparts P and \mathbf{V} of p and \mathbf{v} ; the gradient ∇P is approximated by a difference quotient over adjacent volumes. The regions over which we average are chosen to satisfy several criteria described below.

First, to reduce external boundary effects we average velocities over a box-shaped subset $\Omega^r \subset \Omega$ whose sides are shorter than those of Ω by the factor $1 - r$ on each side, $0 < r < 1/2$.

Second, the difference quotient approximation of each component of ∇P is computed from the averages of pressures p over two adjacent box-shaped subsets of Ω^r , each on an opposite

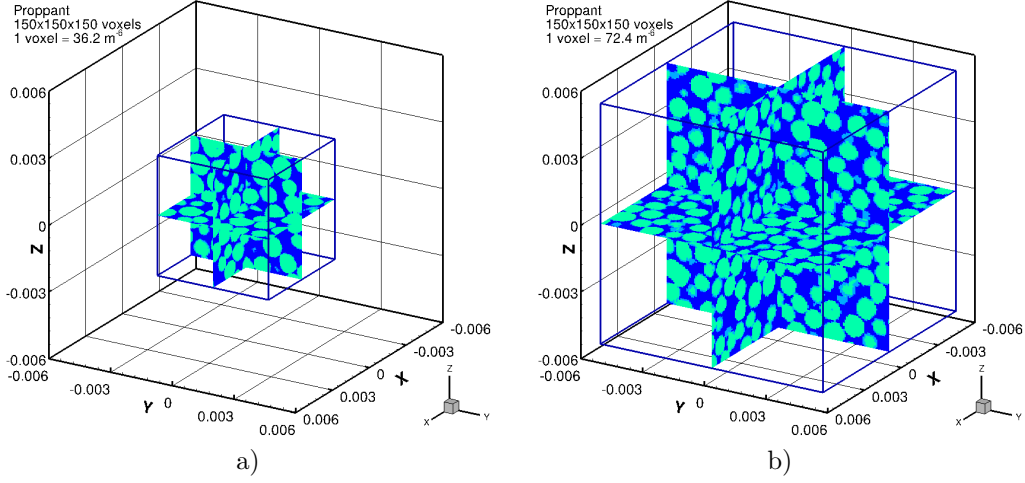


Figure 4: Computational domains, space available for fluid is colored in blue. a) *PROP_red1* was obtained with one reduction of original data, number of voxels $150 \times 150 \times 150$, $h = 36.2 \times 10^{-6} \text{m}$, b) *PROP_red2* was obtained with two reductions, number of voxels $150 \times 150 \times 150$, $h = 72.4 \times 10^{-6} \text{m}$.

side of a plane bisecting Ω^r . Since there are three such planes, one can approximate three components of ∇P . However, if the flow is mostly aligned with the normals to two of the planes, the two components of ∇P aligned with these planes are small but nonzero. For example, if the flow is from left to right, the largest differential of average pressures is from left to right. In our simulations we assign the inflow boundary condition on the left, top, and back sides of the porous region Ω and obtain results for the flow in three independent directions. This yields nine calculated components of velocity and pressure gradients, which can be next used to get the nine components of \mathbf{K} from (5) written for every direction of the flow.

Large flow rates It is well known [31] that the effective conductivity \mathbf{K} in Darcy's law (5) is constant only for slow flow rates for which the Reynolds number \mathbf{Re} is less than \mathbf{Re}_{crit} . Here $\mathbf{Re} = \frac{|\mathbf{v}|\delta\rho}{\mu}$, where δ denotes the characteristic length scale for the flow. For pore-scale flow \mathbf{Re}_{crit} is typically taken between 1 and 10 and δ is the average solid grain size equal to the ratio of volume of solid $|\Omega_s|$ to the surface area $|\Gamma|$ of the solid-void interface [31].

For the flow rates with \mathbf{Re} higher than \mathbf{Re}_{crit} , the effective conductivity \mathbf{K} in (5) depends nonlinearly on the flow rate V , and the model (5) must be extended. The Forchheimer extension of (5) given in [31] that we used in [7] includes the original Darcy term $\mathbf{K}_D \nabla P$ and the inertia term $\beta |\mathbf{V}| \mathbf{V}$ in the form

$$(1 + \beta |\mathbf{V}|) \mathbf{V} = -\mathbf{K}_D \nabla P, \quad x \in \Omega. \quad (6)$$

The presence of $\beta |\mathbf{V}| \mathbf{V}$ makes the model (6) nonlinear and it reflects the fact that the effective conductivity \mathbf{K} decreases with $|\mathbf{V}|$ as in $(\mathbf{K}(\mathbf{V}))^{-1} = \mathbf{K}_D^{-1}(1 + \beta |\mathbf{V}|)$.

The core-scale parameters of (6) can be found by upscaling. In particular, \mathbf{K}_D can be found from a computational experiment at some low flow rate, and the new model parameter β can be found from additional experiments at high flow rates. More generally, we set up simulations for several inlet velocities $v_{in}^{(j)}$, $j = 0, \dots, MAX$ to get \mathbf{K}_D and β , and to confirm that the model (6) is valid. More details and discussion of various extensions of (6) and in particular those accounting for anisotropy of β can be found in [7].

Table 2: Computational grids

dataset	voxels	h $\times 10^6 \text{ m}$	$\#\text{voids}$	$\#\text{solids}$	ϕ	$\#\text{cells}$	δ $\times 10^4$
PROP_red1	$150 \times 150 \times 150$	36.2	1370490	2004510	0.406	10963920	1.07
PROP_red2	$150 \times 150 \times 150$	72.4	1466702	1908298	0.435	11733616	1.10

4 Numerical experiments

With the proppant geometries obtained from imaging described in Section 2 we conducted numerical simulations of the pore-scale flow followed by upscaling as outlined in Section 3. The original voxel grid covering Ω is a grid of $1000 \times 1000 \times 600$ voxels, each of side $h = 18.1 \times 10^{-6} \text{ m}$ long, and this corresponds roughly to $2 \cdot 10^8$ voxels in Ω_F . To keep the mesh size manageable, we reduce the original geometry in one of two ways described in Section 3. The geometry denoted by PROP_red1 is obtained in one coarsening step which reduces the voxel grid to $500 \times 500 \times 300$, and is followed by cropping the sample to a centrally located rectangular volume of size $150 \times 150 \times 150$ voxels with $h = 36.2 \times 10^{-6} \text{ m}$. The geometry denoted by PROP_red2 is obtained with two reduction steps down to the grid of $250 \times 250 \times 150$ voxels, with $h = 72.4 \times 10^{-6} \text{ m}$, and taking a centrally located rectangular volume of size $150 \times 150 \times 150$. We note that the physical dimensions of PROP_red2 are twice as big as those of PROP_red1, but at a price of a poorer resolution. Next, computational mesh is generated for each geometry, with one level of mesh refinement. See Fig. 4 and Table 2 for illustrations and details. Here ϕ denotes porosity of a sample, i.e., the volume fraction $\frac{|\Omega_F|}{|\Omega|}$ of voids in Ω .

Simulation results and conductivity reduction due to high flow rates Next we simulate water flow in the proppant geometries, and set $\rho = 1000 \text{ [kg/m}^3\text{]}$ and $\mu = 1.003 \times 10^{-3} \text{ [kg/m} \cdot \text{s]}$. A sequence of simulations is performed for a range of increasing inlet velocities $v_{in}^{(j)}$, $j = 0, \dots, MAX$. The detailed information on the flow behavior in Fig. 6 shows an evident difference in the flow behavior between small and large flow rates.

Next, for each velocity we compute the averages \mathbf{V} and ∇P and find the effective conductivity \mathbf{K} from Eq. (5). The results are summarized in Table 3 and Fig. 5 where we report the values of diagonal components of computed effective conductivity tensors; the off-diagonal values are very small for this medium and are not reported.

As we see in Table 3, the proppant medium is essentially isotropic, with the tensor components K_{11} , K_{22} and K_{33} very close to one another. In addition, the “baseline” effective conductivity called \mathbf{K}_D in (6) is constant when $\mathbf{Re} < 1$. For \mathbf{Re} starting around 1, a small decrease in conductivity is observed, to become more pronounced as \mathbf{Re} increases to around 100, beyond which the numerical solver has difficulty converging. The decrease of effective conductivity at high flow rates is one of the critical factors reducing the productivity of hydraulically fractured wells.

Furthermore, we can discuss the impact of geometry coarsening and REV size by comparing the results for PROP_red1 and PROP_red2. Consistently, the conductivities computed with the coarser mesh PROP_red2 on a larger domain are larger than those computed with the finer mesh but on a smaller domain PROP_red1; this is correlated with the fact that the coarser voxel grid has larger porosity.

To test the effect of REV size alone, we study the impact of the parameter r in the choice of REV domain Ω^r . We recall that with $r = 0.1$ the length of Ω^r in each direction is 20% smaller than the length of Ω , and $r = 0.25$ corresponds to the region of averaging two times smaller

Table 3: Computed conductivities of the proppant sample.

$v_{in} \times 10^5$	$ \mathbf{V} \times 10^5$	\mathbf{Re}	$K_{11} \times 10^8$	$K_{22} \times 10^8$	$K_{33} \times 10^8$
PROP_red1		REV=0.05			
1	1.015	0.0011	75.85	73.46	78.17
1000	1014	1.065	74.03	70.98	76.06
1e+04	1.002e+04	10.65	49.05	42.96	48.93
7e+04	6.924e+04	74.55	14.79	11.60	14.06
PROP_red1		REV=0.15			
1	0.9976	0.0011	79.63	70.25	75.53
1000	995.1	1.065	78.09	67.61	73.58
1e+04	9878	10.65	52.10	40.93	47.92
7e+04	6.889e+04	74.55	15.85	11.23	13.95
PROP_red1		REV=0.25			
1	0.9718	0.0011	76.38	71.71	71.39
1000	970.7	1.065	75.57	68.91	70.17
1e+04	9693	10.65	52.46	41.14	46.62
7e+04	6.78e+04	74.55	16.13	11.15	13.78
PROP_red2		REV=0.05			
1	1.035	0.00055	96.34	94.09	100.3
1000	1033	0.55	92.48	90.48	96.13
1e+04	1.021e+04	5.50	54.24	53.41	56.36
6e+04	6.079e+04	32.98	16.22	16.00	16.57
PROP_red2		REV=0.15			
1	1.055	0.00055	96.95	95.26	105.9
1000	1052	0.55	93.00	91.52	101.2
1e+04	1.033e+04	5.50	54.28	53.80	58.49
6e+04	6.135e+04	32.98	16.19	16.10	17.12
PROP_red2		REV=0.25			
1	1.042	0.00055	97.87	92.35	103.9
1000	1040	0.55	94.13	88.83	99.52
1e+04	1.03e+04	5.50	55.28	52.41	58.28
6e+04	6.144e+04	32.98	16.54	15.69	17.31

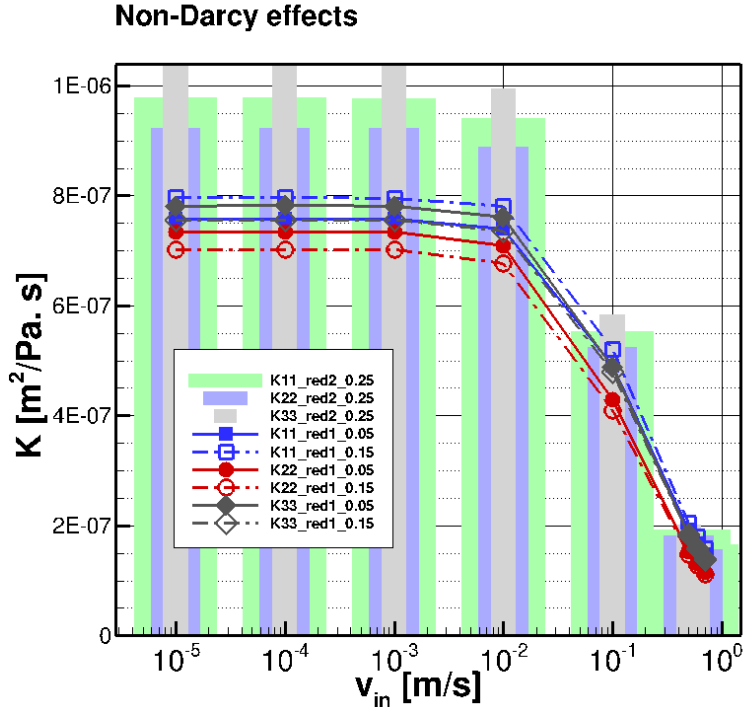


Figure 5: Effects of flow rates on effective conductivity. We compare results obtained for meshes *PROP_red2* (bars) and *PROP_red1*, as well as differences due to different volumes of averaging.

than that of Ω . If the results with different r are very different, this suggests that the smallest REV is not large enough. We see however little dependence on r . Furthermore, the physical size of the region of averaging for *PROP_red2* with $r = 0.25$ is close to that for *PROP_red1* with $r = 0.05$, but the conductivities obtained differ, clearly due to different h and due to the porosity difference. The effect of grid size h alone is discussed next.

Convergence with h A natural question in pore-scale computations and upscaling to core-scale is the influence of the grid size h upon the results. However, the large size of computational mesh for a large enough REV frequently restricts the convergence studies to one level of refinement or to relatively small grids or simple domains as we were able to pursue in [12, 13, 7].

In this paper we consider several levels of grid refinement starting with a subset of the original voxel grid n_{ijk} of size $150 \times 150 \times 150$. We consider flow in the Darcy regime with $v_{in} = 1 \cdot 10^{-5} \text{ m/s}$, and compare the upscaled conductivities \mathbf{K} corresponding to different grids, see Table 4 where *rafk* denotes grid refinement by a factor k with respect to the original voxel grid. For example, one original voxel is replaced with $2 \times 2 \times 2 = 8$ grid cells in the grid *raf2* and with $3 \times 3 \times 3 = 27$ grid cells for grid *raf3*. The conductivities decrease with decreasing h and seem to settle to an asymptotic value for the smallest h . The largest difference is for the first level of refinement, and the convergence to the asymptotic value appears to be approximately of first order.

It is very important to compare the conductivity \mathbf{K} that we computed with the available experimental data. In fact, we first attempted this comparison in [12] but at that time we only had synthetic 2D sand geometries. More recently Scheibe et al. showed in [26] that the

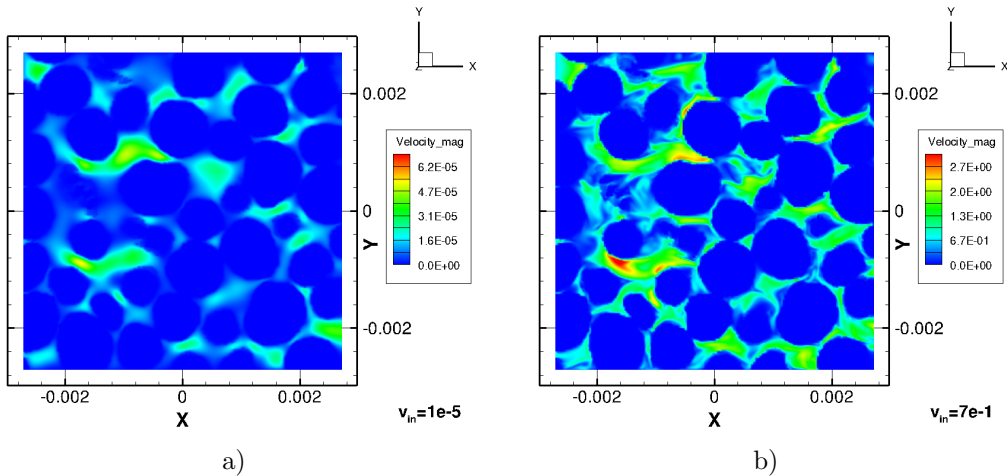


Figure 6: Mesh PROP_red1, cross-section $z = 0$. Velocity field for: a) $\mathbf{Re} \approx 0.001$, b) $\mathbf{Re} \approx 70$.

Table 4: Convergence study

dataset	$h \times 10^6$ [m]	#nodes	#cells	$K_{11} \times 10^8$	$K_{22} \times 10^8$	$K_{33} \times 10^8$
raf1	18.1	1546736	1321687	72.23	58.66	61.58
raf2	9.05	11472341	10573496	66.86	54.23	56.74
raf3	6.03	37706686	35685549	65.55	52.93	55.45
raf4	4.53	88179893	84587968	64.81	52.53	54.87

experimental and computed conductivities for gravel are within an order of magnitude from each other. In [32] we obtained similar agreement for glass-beads and biofilm filled pores. On the other hand, the experimental values of proppant conductivity in [37] indicate that the values of \mathbf{K} for proppants of mesh 16/30 are 100×10^8 , 108×10^8 , and 85.1×10^8 [$\text{m}^2/\text{Pa} \cdot \text{s}$]. These are very close to the \mathbf{K} we present in Table 3 and 4, so the agreement is even closer than that in [26, 32]. Still, we believe that more experiments and more computational studies need to be conducted on well chosen samples.

Changes in pore geometries due to bridging of throats The intrusion of fines into propped fractures severely deteriorates the conductive properties of the proppant material. The pore-scale simulations can be applied to study the effects of the fines on the flow parameters at the core-scale. We distinguish three main types of geometry modifications that may occur regardless of the mechanisms underlying the transport of fines. These are (i) the appearance of “discrete particles” within porespace, (ii) the “pore-lining” causing a relatively uniform narrowing of the throats and pores, and (iii) the “bridging” resulting in the blockage of some throats.

In [13] we studied the effect of pore-lining and in [32] we studied the effect of biofilm and biomass growth causing the pore-lining as well as the appearance of discrete particles. Here we propose a stochastic model inspired by [29] of bridging occurring due to the fines intrusion. We use PROP_red1 (see Table 2) as the initial geometry. Our stochastic model of bridging consists of replacing some of the void voxels with solids, restricting the choice of the voxels only to those in the narrow throats. We control the number of blocked throats with a parameter denoted *rand*. The larger the parameter *rand* is, the more fines are kept in the throats. Fig. 7 shows examples of randomly modified geometries, with the simulated fines marked with red; the details

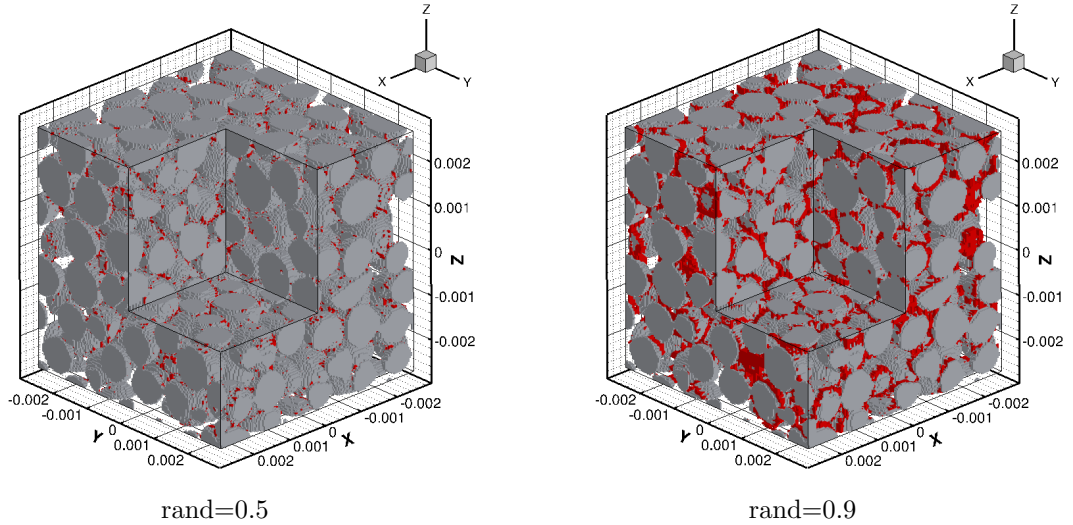


Figure 7: Initial geometry *PROP_red1* (grey) is modified by simulating bridging of throats, with probability parameter *rand*. Accumulated particles are marked in red.

Table 5: Computational grids for throats bridging

dataset	voxels	h $\times 10^6 m$	#voids	#solids	ϕ	#cells	δ $\times 10^4$
PROP_red1							
<i>rand_0.5</i>	$150 \times 150 \times 150$	36.2	1304753	2070247	0.387	10438024	1.04
<i>rand_0.7</i>	$150 \times 150 \times 150$	36.2	1235995	2139005	0.366	9887960	1.17
<i>rand_0.9</i>	$150 \times 150 \times 150$	36.2	1173598	2201402	0.348	9388784	1.33

on the corresponding computational meshes are given in Table 5.

Next we discuss the effects of bridging at core-scale. The effects of throats bridging are visualized in Fig. 9. Bridging causes a small reduction of porosity and a pronounced decrease of the overall conductivity. In some cases of extensive bridging, there may be no percolation through Ω ; this is reported as screenout of a fracture.

The geometries corresponding to increasing parameter *rand* can be interpreted as "snapshots" of the time evolution of the bridging process associated with the fines transport. Thus the conductivities in Table 6 can be seen as data for the deterioration in time of fracture conductivity. Furthermore, our results also cover non-Darcy effects on conductivity.

5 Conclusions

Computer simulations based on real pore-scale images provide a powerful tool for the study of the flow in proppant geometries and of proppant conductivity. In this paper we overviewed the set-up of our virtual laboratory which offers, in spite of various limitations due to the size of datasets, a valuable complement to the true experimental results.

In this work we considered two particular phenomena which can severely reduce proppant conductivity. These are non-Darcy effects present at high velocities, and the effect of bridging

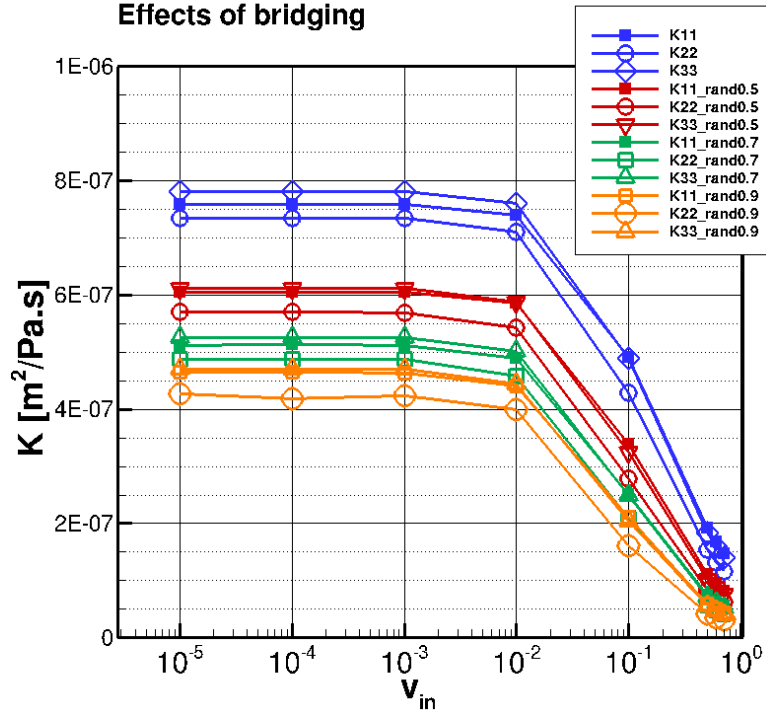


Figure 8: Effective conductivities computed for a sequence of pore-scale geometries representing different level of throats bridging.

Table 6: Conductivity reduction caused by throats bridging

$v_{in} \times 10^5$	$ V \times 10^5$	Re	$K_{11} \times 10^8$	$K_{22} \times 10^8$	$K_{33} \times 10^8$
PROP_red1	rand=0.5	REV=0.05			
1	1.073	0.001	60.54	56.98	61.16
1000	1072	1.04	58.53	54.24	58.84
1e+04	1.057e+04	10.42	33.86	27.81	32.58
7e+04	7.272e+04	72.92	8.234	6.251	7.639
PROP_red1	rand=0.7	REV=0.05			
1	1.134	0.001	51.23	48.78	52.59
1000	1133	1.16	48.93	45.78	50.06
1e+04	1.116e+04	11.64	25.15	20.96	24.90
7e+04	7.638e+04	81.47	5.515	4.237	5.259
PROP_red1	rand=0.9	REV=0.05			
1	1.19	0.001	46.53	42.67	47.05
1000	1188	1.33	44.02	39.99	44.37
1e+04	1.168e+04	13.27	21.04	16.11	20.42
7e+04	7.981e+04	92.92	4.385	3.096	4.093

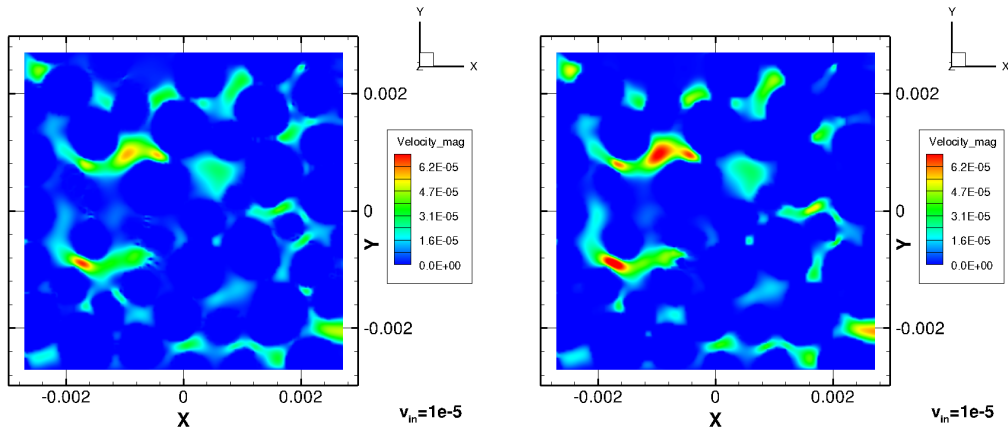


Figure 9: Velocity field at cross section $z = 0$ computed with $v_{in} = 10^{-5} [m/s]$ on mesh PROP_red1 modified by simulating throats bridging with probability $rand = 0.5$ and $rand = 0.9$

of the pore throats due to the fines migration. In the latter project, our choice of voxel-based computational grids is particularly well suited to modelling geometry modifications.

Modeling of conductivity decrease and of the associated pressure increase helps in the study of flow in hydraulically fractured formations. With realistic geometries of proppant samples, our virtual laboratory helps to develop more accurate models for flow processes following the fracturing.

Acknowledgments A. Trykozko has received funding from the Polish-Norwegian Research Programme operated by the National Centre for Research and Development under the Norwegian Financial Mechanism 2009-2014 in the frame of Project Contract No Pol-Nor/209820/14/2013. Her research was in part supported by PL-Grid infrastructure and the computing grant G35-12 of Interdisciplinary Centre for Modeling.

M. Peszynska was partially supported by the grant NSF-DMS 1115827 "Hybrid modeling in porous media".

The authors would like to thank Prof. Ralph Showalter for his valuable comments and the anonymous referees for their suggestions which helped to improve the paper.

Computing resources Computations were performed on the facilities located at ICM. The cluster *hydra* - HP Blade Systems/ Actina Solar, Intel Xeon 5660 architecture x86_64 was used. Most of simulations were performed with 24 processes running in parallel on nodes with 24 GB memory. The largest cases of Table 4 used 72 processes running on Intel E5-2697 v3 (Huawei) cores.

References

- [1] M. Blunt, B. Bijeljic, H. Dong, O. Gharbi, S. Iglauer, P. Mostaghimi, A. Paluszny, C. Pentland, Pore-scale imaging and modeling, *Advances in Water Resources* 51 (2013) 197–216.

- [2] D. Wildenschild, A. Sheppard, X-ray imaging and analysis techniques for quantifying pore-scale structure and processes in subsurface porous medium systems, *Advances in Water Resources* 51 (2013) 217–246.
- [3] M. Andrew, B. Bijeljic, M. Blunt, Pore-by-pore capillary pressure measurements using x-ray microtomography at reservoir conditions: Curvature, snap-off, and remobilization of residual CO₂, *Water Resources Research* 50 (2014) 8760–8774.
- [4] B. Bijeljic, A. Raeini, P. Mostaghimi, M. Blunt, Predictions of non-Fickian solute transport in different classes of porous media using direct simulations on pore-scale images, *Physical Review E* 87 (2013) 013011.
- [5] P. Mostaghimi, M. Blunt, B. Bijeljic, Computations of absolute permeability on micro-CT images, *Mathematical Geosciences* 45 (2013) 103–125.
- [6] G. Narsillio, O. Buzzi, S. Fityus, T. Yun, D. Smith, Upscaling of Navier-Stokes equations in porous media: theoretical, numerical and experimental approach, *Computers and Geotechnics* 36 (2009) 1200–1206.
- [7] M. Peszyńska, A. Trykozko, Pore-to-core simulations of flow with large velocities using continuum models and imaging data, *Computational Geosciences* 17 (4) (2013) 623–645.
- [8] M. Siena, J. Hyman, M. Riva, A. Gaudagnini, C. Winter, P. Smolarkiewicz, P. Gouze, S. Sadhukhan, F. Inzoli, G. Guédon, E. Colombo, Direct numerical simulations of fully saturated flow in natural porous media at the pore scale: a comparison of three computational systems, *Computational Geosciences* 19 (2015) 423–437.
- [9] X. Yang, T. Scheibe, M. Richmond, W. Perkins, S. Vogt, S. Codd, J. Seymour, M. McKinley, Direct numerical simulations of pore-scale flow in a bead pack: comparison with magnetic resonance imaging observations, *Advances in Water Resources* 54 (2013) 228–241.
- [10] M. Peszyńska, A. Trykozko, K. Augustson, Computational upscaling of inertia effects from porescale to mesoscale, in: G. Allen, J. Nabrzyski, E. Seidel, D. van Albada, J. Dongarra, P. Sloot (Eds.), *ICCS 2009 Proceedings, LNCS 5544, Part I*, Springer-Verlag, Berlin-Heidelberg, 2009, pp. 695–704.
- [11] M. Peszyńska, A. Trykozko, Convergence and stability in upscaling of flow with inertia from pore-scale to meso-scale, *International Journal for Multiscale Computational Engineering* 9 (2011) 215–229.
- [12] M. Peszyńska, A. Trykozko, W. Sobieski, Forchheimer law in computational and experimental studies of flow through porous media at porescale and mesoscale, in: *Mathematical Sciences and Applications, GAKUTO International Series*, 2010, pp. 463–482.
- [13] A. Trykozko, M. Peszyńska, Pore-scale simulations of pore clogging and upscaling with large velocities, in: *Mathematical Sciences and Applications, GAKUTO International Series*, 2013, pp. 277–300.
- [14] B. Barree, H. Fitzpartick, J. Manrique, M. Mullen, S. Schubarth, M. Smith, N. Stegent, Proping-up production, in: *Conductivity Endurance*, Halliburton, 2005.
- [15] P. Kasza, Effective fracturing of shales (in Polish), *NAFTA-GAZ (Oil-Gas)* 11 (2013) 807–813.

- [16] M. Vincent, Five things you did not want to know about hydraulic fractures, in: A. Bungler, J. McLennan, R. Jeffrey (Eds.), *Effective and Sustainable Hydraulic Fracturing*, InTech, 2013.
- [17] S. Holditch, R. Morse, The effects of non-Darcy flow on the behavior of hydraulically fractured gas wells, *Journal of Petroleum Technology* (1976) 1169–1179.
- [18] T. Giorgi, Derivation of the Forchheimer law via matched asymptotic expansions, *Transport in Porous Media* 29 (1997) 191–206.
- [19] C. Garibotti, M. Peszyńska, Upscaling non-Darcy flow, *Transport in Porous Media* 80 (2009) 401–430.
- [20] J. Kaczmarczyk, M. Dohnalik, J. Zalewska, Evaluation of carbonate rock permeability with the use of X-ray computed microtomography, *NAFTA-GAZ (Oil-Gas)* 4 (2011) 233–238.
- [21] J. Zalewska, J. Kaczmarczyk, Analysis of rock samples’ internal pore structure based on X-ray computed microtomography data, part I, *NAFTA-GAZ (Oil-Gas)* 8 (2011) 533–544.
- [22] X-tek (Nikon), User Manual for version 1.0.2911.19153.
- [23] FEI, www.fei.com/software/avizo3d/, Avizo 3D Software User’s Guide.
- [24] Fraunhofer Institute for Industrial Mathematics, www.itwm.fraunhofer.de/en/departments-/image-processing/microstructure-analysis/mavi.html, MAVI - Modular Algorithms for Volume Images.
- [25] A. Raeni, M. Blunt, B. Bijeljic, Modelling two-phase flow in porous media at the pore scale using the volume-of-fluid method, *Journal of Computational Physics* 231 (2012) 5653–5668.
- [26] T. Scheibe, W. Perkins, M. Richmond, M. McKinley, P. Romero-Gomez, M. Oostrom, T. Wietsma, J. Serkowski, J. Zachara, Pore-scale and multiscale numerical simulation of flow and transport in a laboratory-scale column, *Water Resources Research* 51 (2015) 1023–1035.
- [27] M. Siena, A. Guadagnini, M. Riva, B. Bijeljic, J. P. Nunes, M. Blunt, Statistical scaling of pore-scale Lagrangian velocities in natural porous media, *Physical Review E* 90 (2014) 023013.
- [28] R. Al-Raoush, C. Willson, Extraction of physically realistic pore network properties from three-dimensional synchrotron X-ray microtomography images of unconsolidated porous media systems, *Transport in Porous Media* 300 (2005) 44–64.
- [29] P.-E. Øren, S. Bakke, Process based reconstruction of sandstones and prediction of transport properties, *Transport in Porous Media* 46 (2002) 311–343.
- [30] ANSYS, Inc., ANSYS FLUENT User’s Guide, Rel. 15.0 (2014).
- [31] J. Bear, A. Cheng, *Modeling Groundwater Flow and Contaminant Transport*, Springer, 2010.
- [32] M. Peszynska, A. Trykozko, G. Iltis, S. Schlueter, D. Wildenschild, Biofilm growth in porous media: experiments, computational modeling at the porescale, and upscaling, *Advances in Water Resources* (2015), doi:10.1016/j.advwaters.2015.07.008.

- [33] L. Tartar, Incompressible fluid flow in a porous medium—convergence of the homogenization process, in: *Nonhomogeneous media and vibration theory*, Vol. 127 of *Lecture Notes in Physics*, Springer-Verlag, Berlin, 1980, pp. 368–377.
- [34] L. Dormieux, D. Kondo, Approche micromécanique du couplage perméabilité-endommagement, *Comptes Rendues Mecanique* 332 (2004) 135–140.
- [35] T. Abdalrahman, S. Scheiner, C. Hellmich, Is trabecular bone permeability governed by molecular ordering-induced fluid viscosity gain? arguments from re-evaluation of experimental data in the framework of homogenization theory, *Journal of Theoretical Biology* 365 (2015) 433–444.
- [36] L. Durlofsky, Numeric calculation of equivalent grid block permeability tensors for heterogeneous porous media, *Water Resources Research* 27 (1991) 600–708.
- [37] Saint-Gobain Proppants, www.proppants.saint-gobain.com/sites/default/files/Shale-Brochure.pdf/.